Planar delamination behaviour of CFRP panels under quasi-static out-of-plane loading

Tu, Wenjie; Pascoe, John Alan; Alderliesten, René

DOI
10.1016/j.compstruct.2024.118137

Publication date
2024

Document Version
Final published version

Published in
Composite Structures

Citation (APA)
Tu, W., Pascoe, J. A., & Alderliesten, R. (2024). Planar delamination behaviour of CFRP panels under quasi-static out-of-plane loading. *Composite Structures*, *339*, Article 118137. https://doi.org/10.1016/j.compstruct.2024.118137

Composite Structures 339 (2024) 118137

Contents lists available at ScienceDirect

Composite Structures

journal homepage: www.elsevier.com/locate/compstruct

Planar delamination behaviour of CFRP panels under quasi-static out-of-plane loading

Wenjie Tu *, John-Alan Pascoe, René Alderliesten

Department of Aerospace Structures and Materials, Faculty of Aerospace Engineering, Delft University of Technology, Kluyverweg 1, Delft, 2629HS, The Netherlands

ARTICLE INFO

Dataset link: https://doi.org/10.4121/8ca918e1-4423-499e-be19-174562fa6973

Keywords:
Polymer-matrix composites (PMCs)
Delamination
Delamination migration
Finite element analysis (FEA)

ABSTRACT

In this study, a novel experimental approach was devised to investigate shear dominant and combined opening-shear planar delamination behaviours in composite laminates subjected to quasi-static out-of-plane loading. The patterns of planar delamination growth were depicted through different inspection techniques, including digital image correlation (DIC), C-scan, and microscopic observation. The artificially embedded delamination propagated in the direction parallel to the fibre orientation of the layer above the mid interface, but migrated to an upper interface in the direction transverse to the directing ply. A continuous stiffening process was recognized with increasing delamination area. Furthermore, a numerical analysis based on virtual crack closure technique (VCCT) indicated that the local mode II was dominant for delamination growth, while the local mode III triggered delamination migration.

1. Introduction

As one of the most typical damage types in CFRP laminates, delamination growth causes significant strength and stiffness degradation, thus threatening the structural integrity [1,2]. Standard evaluation methods have been successfully developed to characterize the delamination behaviour of different fracture modes based on linear-elastic fracture mechanics [3–5]. These experimental methods, which can be referred to as one-dimensional (1-D) tests where delamination is forced to propagate in one direction, are prone to quantify the fracture resistance of unidirectional (UD) laminates since the damage mode is simple. However, the findings derived from the application of standardized one-dimensional methodologies lack generalizability for characterizing planar delamination behaviour in actual structural systems, primarily attributable to the simplification of test configurations and the omission of considerations regarding the intricate nature of multidirectional delamination propagation.

In addition to the standardized tests, research efforts have been made to investigate the effects of stacking sequence [6–9] and loading conditions [10,11] on 1-D delamination behaviour. A characteristic damage mechanism of multi-directional (MD) composite laminates that is absent in UD laminates is delamination migration. The migration behaviours of $0^{\circ}//\theta$ interfaces under different loading conditions (mode I [7,12–16], mode II [17,18], and mixed-mode [8,19–21]) have been studied experimentally and numerically. Besides migration, fibre bridging was associated with tortuous delamination growth, causing an increasing R-curve behaviour [9,18,21–23]. Although these studies provided insights into the migration mechanism, they were still based on 1-D delamination tests. Delamination growth was forced to propagate across the fibres at an angle of the ply orientation in MD laminates, triggering different degree of ply splits and fibre bridging along the delamination path [7]. This might not apply to planar delamination, where the delamination direction tends to align with the directing ply [6,24,25].

A semi-complex configuration was proposed to investigate planar delamination behaviour in composite panels with embedded defects. Among those, buckle-driven delamination behaviour of CFRP panels has received considerable attention during the past few decades [25–31]. The buckling-induced delamination growth, which was transverse to the loading direction, was found to have close interaction with matrix cracking and ply splits, causing local buckling and thus affecting the global buckling behaviour. The fibre orientation at the major delamination interface had a significant effect on the direction of delamination growth and migration behaviour [25,32].

Since it was difficult to acquire the fracture parameters directly through experiment, qualitative and quantitative analysis of the planar delamination behaviour is limited. Therefore, analytical and numerical methods have been proposed to investigate the strain/stress state and local fracture mode at the delamination front.

Köllner [30,31] developed an analytical model to predict the critical strain for buckle-driven delamination growth based on the estimated

* Corresponding author.
E-mail address: W.Tu@tudelft.nl (W. Tu).

https://doi.org/10.1016/j.compstruct.2024.118137
Received 16 October 2023; Received in revised form 1 March 2024; Accepted 16 April 2024
Available online 23 April 2024

local energy release rate (ERR). Although the prediction matched the experimental results, it was still insufficient to characterize progressive matrix cracking and delamination migration associated with delamination growth. To investigate planar delamination behaviour under mode I loading condition, an experimental and numerical study was performed by Cameselle-Molares et al. [33,34]. According to the numerical investigation based on cohesive zone model (CZM), a 50% increase in the total strain energy release rate (SERR), due to the effects of in-plane stretching and progressive fibre bridging, was achieved in comparison with that from double cantilever beam (DCB) tests [34]. Another experimental investigation of 2-D mode II delamination in GFRP composite laminates has shown a longer fracture process zone (FPZ) in 2-D delamination compared to 1-D [35]. Three stages in the mode II planar delamination growth were recognized, including delamination initiation, slow propagation, and rapid propagation. An early study of Chatterjee's [36] used a three-point bending test to investigate shear dominant planar delamination behaviour of CFRP panels with two elliptical pre-cracks. The analysis of the local SERR distribution provided insights into the mechanisms of delamination growth and migration. Efforts have also been made to explore planar delamination behaviour in CFRP laminate panels under quasi-static and fatigue out-of-plane indentation [37]. However, no detailed interpretation of the observed planar delamination behaviour was provided since the delamination growth was insufficient. There is still a lack of a qualitative and quantitative evaluation method for characterizing planar delamination behaviour of composite laminates.

Therefore, in this study, a novel experiment is proposed in order to characterize planar delamination behaviour of CFRP composite laminates under out-of-plane indentation. Two specimen configurations are designed to examine planar delamination behaviour under mode II and mixed-mode I/II loading conditions. To explore the effect of different interfacial properties on the delamination behaviours, 0°//0° and 0°//90° interfaces are considered. The pattern of delamination growth was captured through 3D DIC analysis , ultrasonic scanning (C-scan) , and cross sectional microscopy. In addition, initiation of delamination growth and the corresponding critical load were determined using an acoustic emission (AE) system , which provides a reference critical displacement value for the initiation point of delamination growth. Furthermore, a numerical analysis is conducted employing a combined approach of the virtual crack closure technique (VCCT) and 3D Hashin damage criterion. The numerical investigation aims to understand the driving force governing both planar delamination growth and delamination migration at the initiation point, rather than simulating the progressive damage process. This research provides a comprehensive analysis of the underlying mechanisms that control planar delamination, thereby explaining the factors that contribute to in-plane growth and migration in order to advance the assessment methodologies for evaluating damage states and propagation behaviours in CFRP composite laminates.

2. Experimental method

2.1. Material and specimen

The material used for manufacturing the specimens was the unidirectional carbon fibre prepreg, M30SC-150-DT120-34F, provided by Delta Tech Italy. The DT120 is a high toughened system suitable for structural components of high impact performance and energy absorption requirements. The material properties are provided in Table 1.

Two distinct specimen configurations, named planar central loaded split (PCLS) and planar central loaded opening (PCLO), were designed to investigate shear dominant and opening-shear delamination behaviours, as illustrated in Fig. 1. For PCLO specimens, a circular hole of 14 mm diameter was cut from the prepregs prior to curing. A plastic cylinder with the same diameter as the hole was embedded before curing to maintain the shape of the opening. In order to introduce the pre-crack, a single layer of Polytetrafluoroethylene (PTFE) with 18 mm diameter and 0.016 mm thickness, was embedded at the middle interface for both types of specimens. The interfaces of interest are 0°//0° and 0°//90°. Two different quasi-isotropic stacking sequences with 16 plies were used in this research, as described in Table 2. The upper and lower sub-laminates were balanced and symmetrical, mitigating undesired deformation due to the coupling of extension/bending/twisting.

Table 1
Material properties of M30SC-150-DT120-34F prepreg [38].

Mechanical properties	Test method	Value
Longitudinal tensile strength, X_T (MPa)	ASTM D 3039	3010.0
Longitudinal tensile modulus, $G_{11,T}$ (GPa)	ASTM D 3039	145.0
Transverse tensile strength, Y_T, Z_T (MPa)	ASTM D 3039	39.0
Transverse tensile modulus, $G_{22,T}$, $G_{33,T}$ (GPa)	ASTM D 3039	6.4
Longitudinal compression strength, X_C (MPa)	ASTM D 6641	1020.0
Longitudinal compression modulus, $G_{11,C}$ (GPa)	ASTM D 6641	133.0
Transverse compression strength, Y_C, Z_C (MPa)	ASTM D 6641	138.0
Transverse compression modulus, $G_{22,C}$, $G_{33,C}$ (GPa)	ASTM D 6641	8.1
In-plane shear strength, S_{12}, S_{13} (MPa)	EN 6031	95.6
In-plane shear modulus, G_{12}, G_{13} (GPa)	EN 6031	3.38
Inter-laminar shear strength, S_{23} (MPa)	EN 2563	77.2

Table 2
Specimen configurations, symmetrical laminates are denoted by $_S$ and the PTFE insert is indicated by //.

Specimen label	Stacking sequence
PCLO(0//0)	$[(0/90/45/-45)_s//(0/90/45/-45)_s]$
PCLO(0//90)	$[(90/0/45/-45)_s//(0/90/45/-45)_s]$
PCLS(0//0)	$[(0/90/45/-45)_s//(0/90/45/-45)_s]$
PCLS(0//90)	$[(90/0/45/-45)_s//(0/90/45/-45)_s]$

2.2. Experimental setup

The experiment setup is shown in Fig. 2. The specimen was fully constrained by the clamps with a rubber mat placed at the contact area at both sides, preventing the specimen from slipping. An indenter with 12 mm diameter and a slight curvature on the head was used. Additionally, the same type of rubber mat (with 1.5 mm thickness) was placed between the indenter and the PCLS specimens to further distribute the applied loading [35]. Based on a preliminary numerical assessment of the loading and the size of the fixture, an MTS machine with 15 kN load cell was chosen. Quasi-static tests were conducted under displacement control with a loading rate of 0.01 mm/s, with a data acquisition frequency of 10 Hz.

In order to visualize planar delamination growth, different inspection methods were integrated in the experimental system as shown in Fig. 2-(b). 3D digital image correlation (3D DIC) technique was used to continuously capture the surface information throughout the loading process (Fig. 2-(c)). According to the recommendations of Correlated Solutions, Inc., a random speckle pattern was applied at the top surface of the panel for DIC analysis. Two cameras with a 23 mm focal length were installed on the top of the crosshead of the MTS test frame. The speckle images were taken every 5 s. The 3D DIC also provided measurement of the true out-of-plane displacement (referred to as "deflection" in the following text) of the PCLS-R specimens. After testing, different C-scan devices were used to capture the delaminated area. First, through-transmission ultrasonic scanning system was used to capture the entire projected delamination area based on signal attenuation, establishing reference data for DIC measurements. In order to capture the delamination depth, pulse-echo ultrasonic scanning facilitated by the Dolphitech technology (Dolphicam2 platform) was employed. This method furnished time-of-flight (TOF) images featuring a colour-coded thickness mapping. Finally, cross-sectional observations were

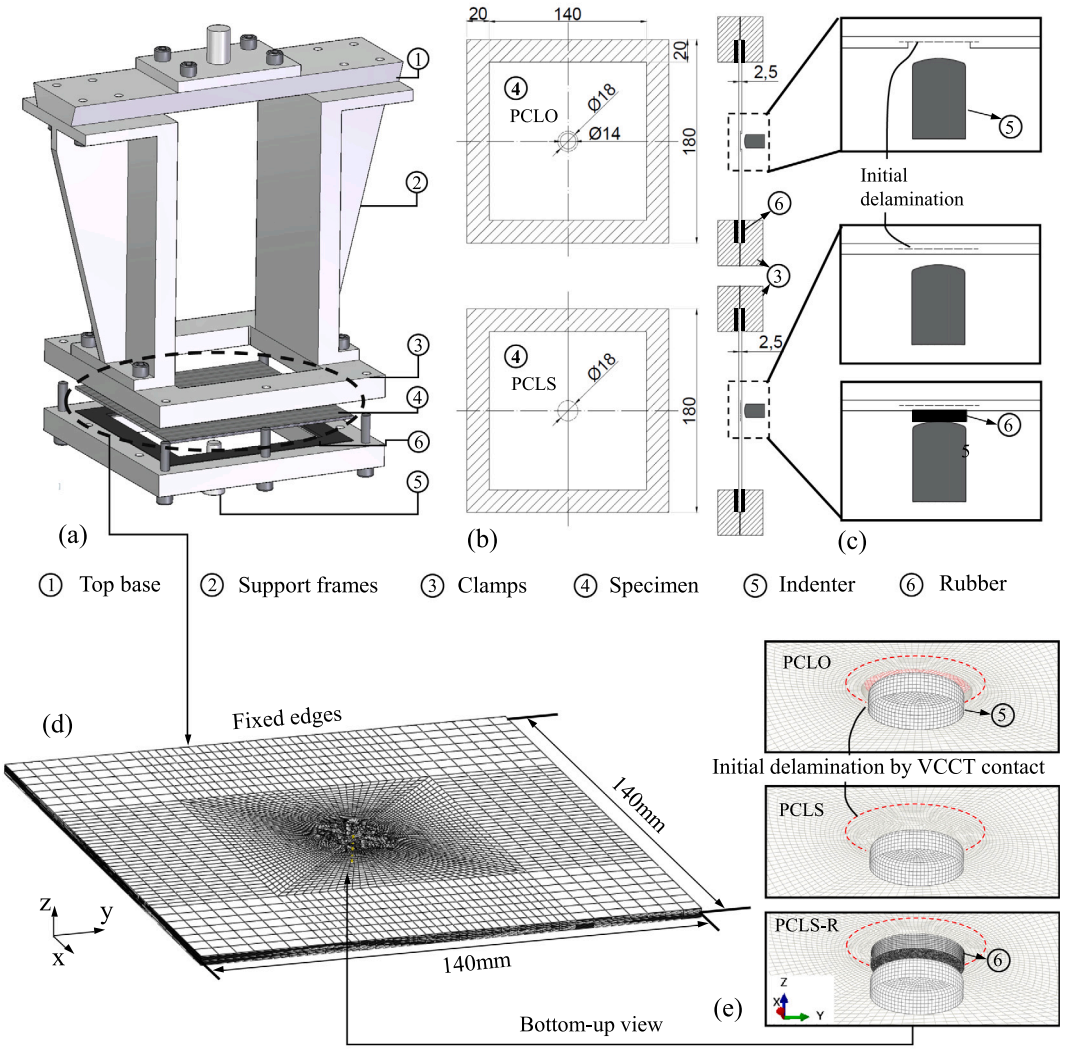

Fig. 1. Illustration of the specimen configurations with (a) the fixtures, (b) specimen geometries, (c) detailed specimen types, (d) numerical model.

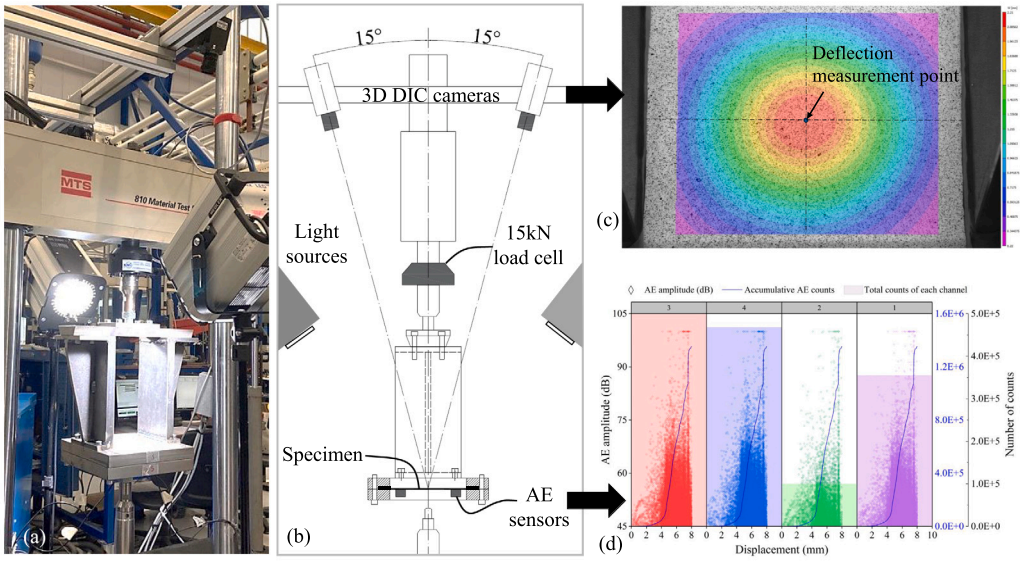

Fig. 2. (a) Experiment setup, (b) schematic of the instrumentation layout, (c) DIC measured surface displacement field, (d) Recorded AE events.

also performed with a KEYENCE VK-X3000 laser confocal microscope to investigate the mechanisms of planar delamination.

An AE system with four sensors attached at the bottom of the specimens was used to detect the initiation of the embedded delamination, as illustrated in Fig. 2-(d). The AE sensors (Vallen Systeme, VS900-M) with a high sensitivity over a wide frequency range were used. The sampling rate for AE recordings was 10 MHz. The AE data was analysed to determine the critical load and provide reference to the initial state of delamination initiation for numerical investigation.

2.3. Experimental procedure

For PCLO specimens, two different loading strategies were applied: single step and multi-step. For single step test, the displacement was increased monotonously until failure of the specimen. In the multi-step tests, the displacement was increased to a pre-defined level, after which the specimen was removed from the fixture and scanned to track delamination growth. The specimen was then reassembled in the fixture and loaded to a higher displacement level. Before starting each step, the specimens were loaded to 20 N to ensure an initial contact. The initial 20 N force was set to be the zero point in the force–displacement behaviour. This process was repeated with incremental displacement levels until failure. For PCLS specimens, only the single step tests were conducted. Additionally, a pre-loading procedure was executed to induce a separation between the PTFE insert and the sub-laminates, introducing a proper pre-crack for all specimens.

3. Numerical modelling

In order to provide insights into the mechanisms of planar delamination behaviour, a finite element (FE) model was developed by using Abaqus, as illustrated in Fig. 1-(d). The virtual crack closure technique (VCCT) was used to extract the distributions of local SERRs and stress tensors, enabling qualitative analysis of the local fracture mode. To prevent shear locking due to bending deformation, 3D linear elements of 8 nodes with incompatible modes (C3D8I) were used for the upper and lower sub-laminates parts. The mid interface between the two parts was bonded by introducing the VCCT contact except for the region of the PTFE insert. The mesh size is set to 0.45 mm at the delamination front, and is subsequently increased to 2.5 mm within the central region to optimize computational efficiency by reducing the number of elements. Since the main objective of this study does not involve an exhaustive modelling of the progressive damage process, delamination growth was not allowed in VCCT by setting $G_{ic} = 10000\ \mathrm{kJ/m^2} (i = I, II, III)$. The local SERRs were calculated based on a one-step VCCT method which used a fixed coordinate system aligned with the directing ply [39] to provide an intuitive illustration of the dominant fracture mode at the initial delamination front.

To simulate the occurrence of possible intra-laminar damage, a 3-D Hashin-type criterion was implemented through an Abaqus user-subroutine (UMAT) [40,41]. In order to differentiate two types of intra-laminar damage, the delamination failure criterion was replaced by a concise failure criterion proposed by Huo [42]. The criterion suggested that only the shear stress component σ_{13} dictated matrix cracking along the fibre direction in a shear dominant damage scenario. In the current study, the effects of the opening stress σ_{33} on delamination type of failure was not negligible for PCLO specimens. The criterion was therefore, modified to the following form:

$$\begin{cases} \sqrt{\left(\dfrac{\sigma_{33}}{Z_T}\right)^2 + \left(\dfrac{\sigma_{13}}{S_{13}}\right)^2} \geq 1, & \text{if } \sigma_{33} \geq 0 \\ \left|\dfrac{\sigma_{13}}{S_{13}}\right| \geq 1, & \text{if } \sigma_{33} < 0 \end{cases} \tag{1}$$

For the specimen with rubber protection, the rubber mat was modelled using 6-node hybrid elements (C3D6H) with a hyperelastic material behaviour. The average mesh size of the rubber part is 0.2 mm. The polynomial properties of strain energy potential of the rubber material were adopted. The material properties of the rubber were numerically adjusted to fit the hyperelastic behaviour, $C_{10} = 4$, $C_{01} = 0.03$, and $D_{01} = 0.001$ [43]. A friction parameter with a value of 0.3 was set in the contact properties and assigned to the rubber/indenter and rubber/specimen interfaces.

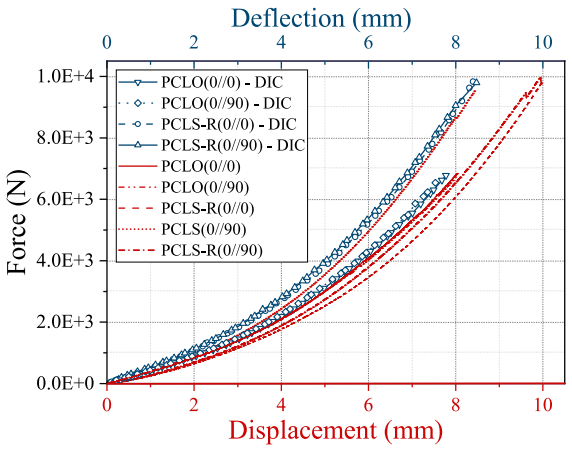

Fig. 3. Force–displacement curves of the specimens subjected to single step loading. PCLS-R denotes the specimens with rubber protection.

4. Results

4.1. Force–displacement behaviour and compliance analysis

The force–displacement curves are shown in Fig. 3. The force was plotted against both the deflection measured by DIC analysis and the displacement applied by the MTS machine. According to Fig. 3, the reaction force increased exponentially as the out-of-plane displacement increased, revealing a constant stiffening process in all specimens. The force–deflection curves of PCLO specimens exhibits good concurrence with the force–displacement curves, indicating that the deflection measured by DIC is reliable in terms of representing the true out-of-plane deformation of the specimens. For PCLS-R(0//90) specimen, the force–deflection curve also shows good agreement with the force–displacement curve of PCLS(0//90) without rubber mat. The force–deflection curves effectively mitigates the influence of the rubber on the force–displacement response of PCLS-R specimens. To distinguish between PCLS-R and PCLO specimens, “deflection” is used to denote true out-of-plane deformation for PCLS-R specimens. The term “displacement” is employed for PCLO specimens, given the equivalence between deflection and displacement in this type of specimens.

To provide clearer illustration of the stiffening process, the compliance and stiffness variations were calculated and were plotted against the displacement for PCLO specimens, and the deflection for PCLS-R specimens. Note that the compliance and stiffness of PCLS-R specimens were calculated based on the deflection of the specimens instead of the applied displacement by MTS machine. As shown in Fig. 4(a), the compliance of all specimens decreased as the displacement/deflection increased. Initially, the PCLS(0//90) specimen demonstrates a compliance level similar to that of the PCLO specimens. However, with increasing loading, a more rapid decrease in the compliance of the PCLS(0//90) specimen is illustrated. By eliminating the influence of the rubber on the stiffness of the system, the PCLS-R specimens exhibit an overall higher stiffness in contrast to the PCLO specimens, while exhibiting a good alignment with the behaviour of PCLS(0//90) at higher loading level (Fig. 4(b)). The compliance and stiffness, computed from the displacement data obtained via the MTS machine, displayed heightened sensitivity to the instant change

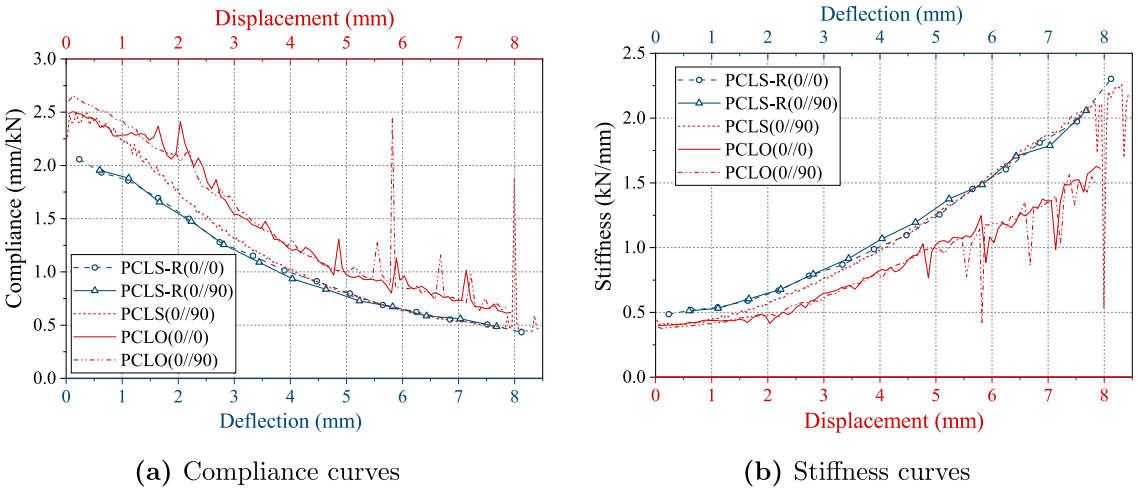

(a) Compliance curves (b) Stiffness curves

Fig. 4. Compliance and stiffness variation of specimens subjected to single step loading.

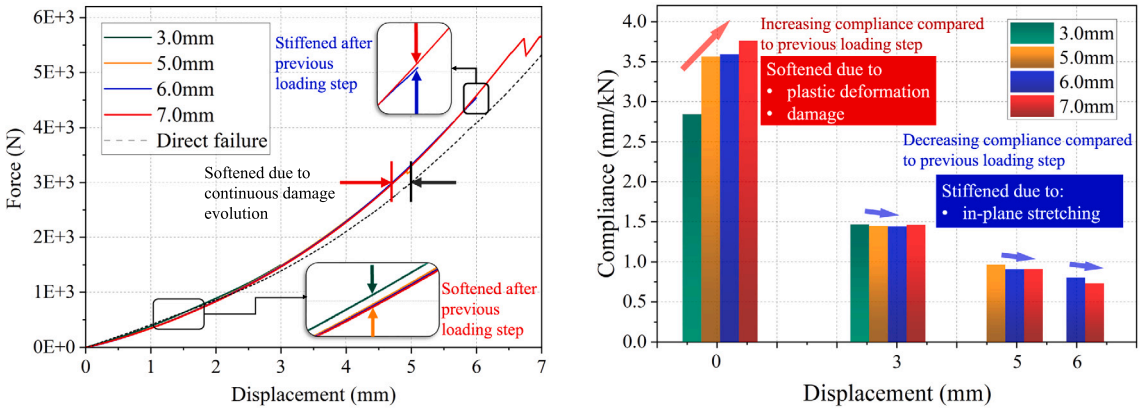

(a) Force-displacement curves (b) Compliance variation

Fig. 5. Force–displacement and compliance curves of PCLO(0//0) specimen subjected to multi-step loadings.

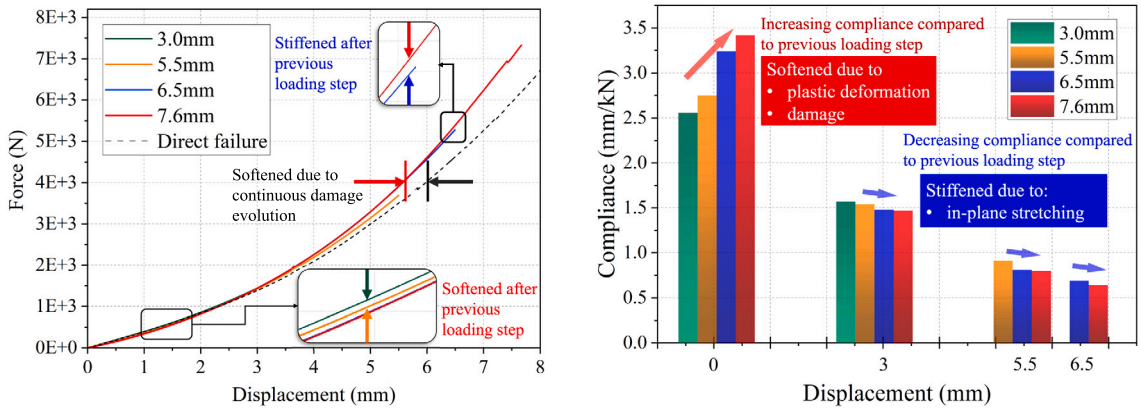

(a) Force-displacement curves (b) Compliance variation

Fig. 6. Force–displacement and compliance curves of PCLO(0//90) specimen subjected to multi-step loadings.

in the force–displacement behaviour. The peaks and drops in the compliance and stiffness curves actually corresponded to surface cracking. However, delamination growth did not cause significant degradation in the stiffness. The force continued to increase after the occurrence of surface cracking.

Similar stiffening process can be observed for PCLO specimens subjected to multi-step loadings. As shown in Figs. 5(a) and 6(a), the curves with different colours indicates different loading steps with different load levels. For single step test of direct failure, the damage evolution with increasing displacement resulted in a more softened

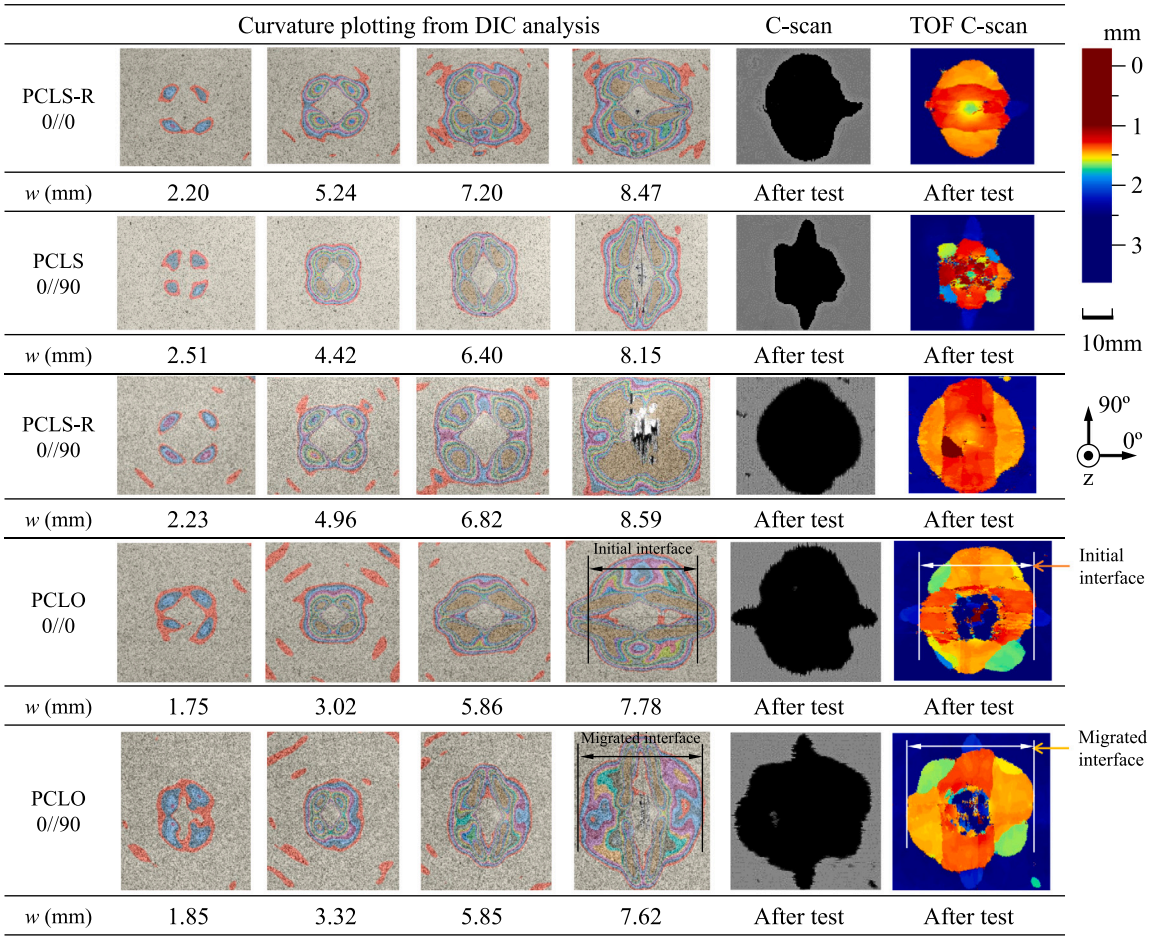

Fig. 7. Delamination patterns captured by different measurement techniques. The coordinates indicates the scanning side of TOF C-scan: from the bottom (indenter side) to the top (DIC side) for all specimens. The colour bar on the right indicates the depth of TOF C-scan. The deep red colour indicates the damage close to bottom surface, while the deep blue colour indicates the top surface. w indicates the out-of-plane deflection measured by DIC.

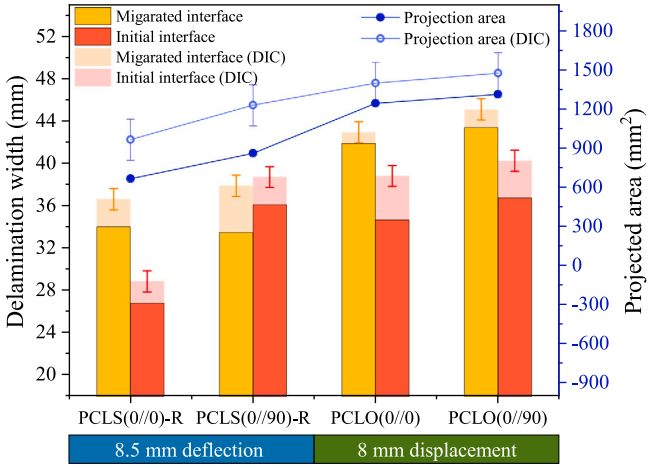

Fig. 8. Comparison of delamination growth of all specimens measured by DIC and C-scan after testing. The error bar in the DIC measurement was conservatively established at ±2 mm, a reflection of the challenges posed by the limited precision in determining the delamination boundary. The bottom columns indicate the true maximum out-of-plane deflection at which delamination growth was measured.

force–displacement behaviour (as shown by the dash line). For multi-step tests, within a lower displacement range, the force–displacement curve shifted downwards from that of the previous loading step, which is ascribed to the presence of pre-existing damage within the specimen. However, as displacement increased, the force–displacement curves exhibit a notable upward shift compared to the previous loading step. As illustrated in Figs. 5(b) and 6(b), the small differences in compliance can be attributed to misalignment of the specimen assembly for different loading steps. However, there is no significant degradation in the overall stiffness of the specimens despite a larger initial delamination has been formed.

4.2. Planar delamination patterns

Planar delamination patterns of five specimens configurations subjected to the single step loading are shown in Fig. 7, while the delamination patterns of the PCLO specimens subjected to multi-step loading are shown in Fig. 10. The 3D DIC analysis and the through transmission C-scan were utilized to capture the projected delamination area, while the TOF C-scan was capable of capturing delaminations at different depths. Significant surface cracking along the fibre direction of the top layer was captured with DIC cameras, and was defined as specimen failure as it caused rapid decrease in stiffness.

With 3D DIC analysis, the planar delamination process was monitored according to the variation in the surface curvature. Although the delaminated region was vague with lower deflection, the presented contour of the surface curvature at the maximum loading corresponded well with the C-scan results. Through TOF C-scan, the growth of the embedded delamination can be observed by filtering the close-to-surface

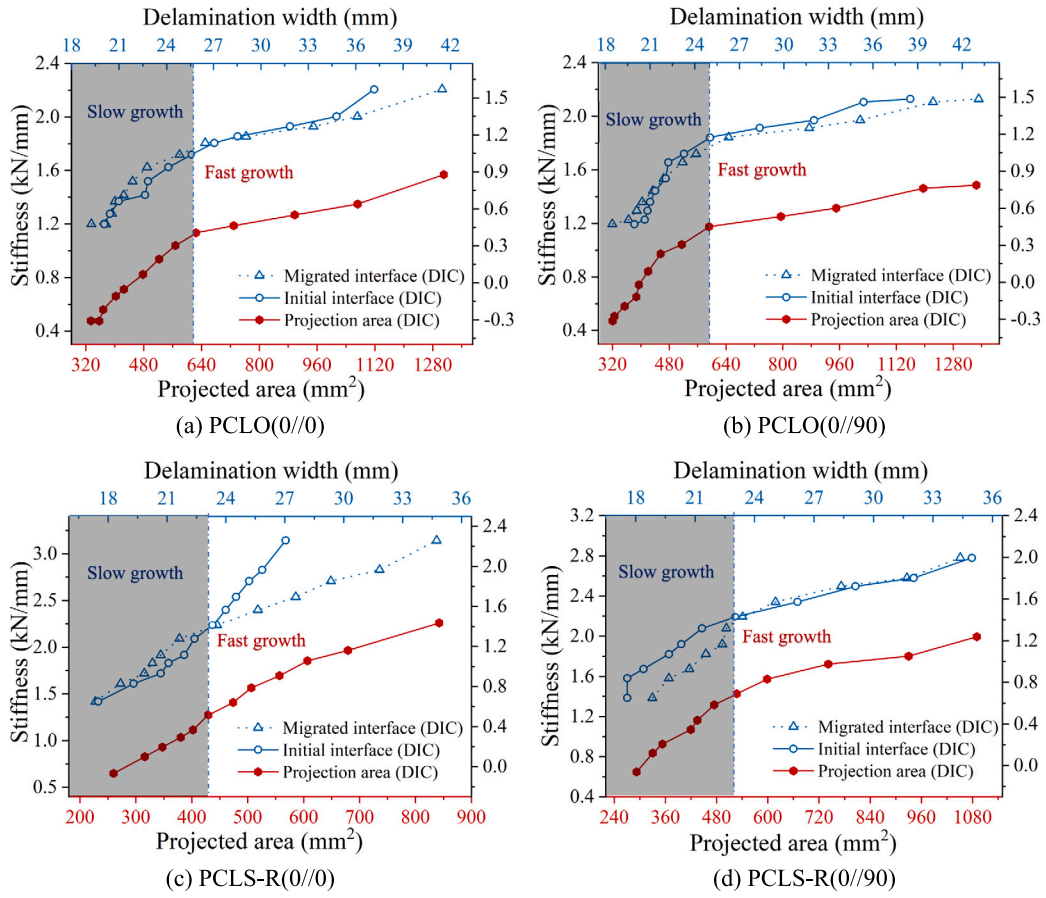

Fig. 9. Stiffness variation of all specimens with delamination growth.

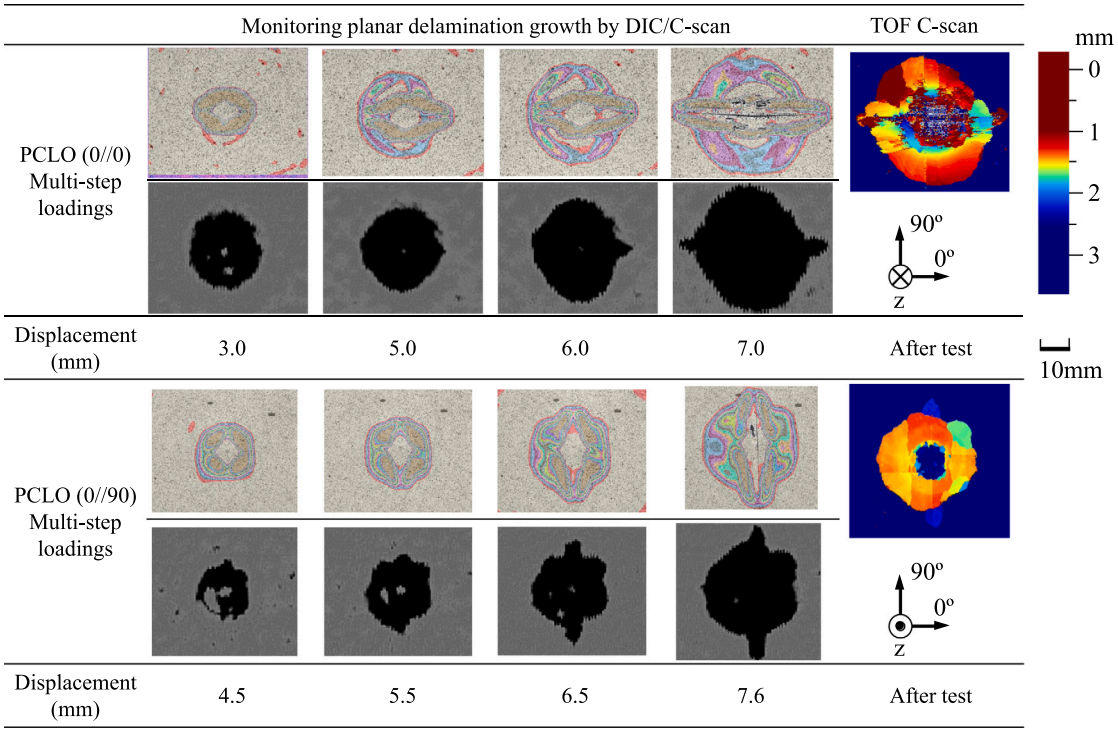

Fig. 10. Delamination patterns of specimens subjected to multi-step loadings.

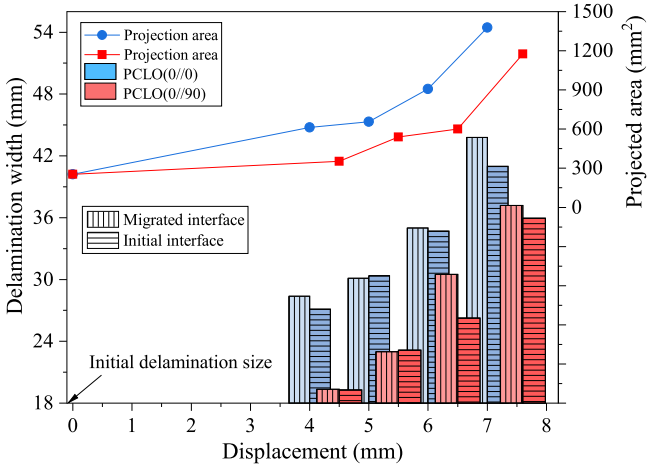

Fig. 11. Comparison of delamination growth of PCLO specimens measured by C-scan at different displacement level.

damage. A clear delamination pattern was observed in PCLS-R specimens compared to PCLS(0//90) specimen without rubber protection. Multiple delaminations occurred at different interfaces in PCLS(0//90) specimen as shown in different colours in TOF C-scan image. In contrast to PCLS-R(0//0), larger delamination growth was observed in PCLS-R(0//90). The embedded delamination growth mainly consisted of three parts. First, a rectangular shape delamination shown in deep orange, of which the width was approximately the same as the diameter of the embedded delamination. Second, the symmetrical semicircle delamination area which initiated from the boundary of the rectangular delamination, as shown in light orange. The two parts were actually positioned at two adjacent interfaces according to the thickness colour map. The first part was recognized as embedded delamination growth along the ply orientation above the mid interface, while the second part represented migrated delamination growth along an adjacent upper ply. The planar delamination patterns of different initial interfaces were the same but 90° rotated.

The amount of the initial and migrated delamination growth (measured as the maximum delamination width at two interfaces), together with the projected delamination area was measured according to the DIC and C-scan images, respectively. As shown in Fig. 8, delamination growth measurements obtained through various inspection methods exhibit consistent trends, even in the presence of inherent measurement errors in DIC analysis due to the vague delamination boundary. Although with lower loading level, the delamination growth observed in PCLO specimens surpassed that of the PCLS specimens. The difference between DIC and C-scan measurements can be attributed to the following factors: first, the unclear correlation between the surface curvature and the actual interlaminar delamination; second, the marginal distortions within the DIC images due to the usage of angled camera settings. In addition, DIC measured delamination area based on surface curvature is not capable of identifying and measuring delaminations at different interfaces, resulting in an underestimation of the total delamination area when an overlapping of multiple delaminations presents. A comprehensive analysis is imperative to address these challenges within the DIC measurement to achieve higher accuracy in measurement of delamination growth with DIC analysis.

Despite the factors mentioned above, the delamination growth was roughly measured using DIC throughout the loading process and correlated with the stiffness variations. As shown in Fig. 9, a consistent delamination growth pattern is observed across different specimen configurations, which can be separated into slow and fast growth stages. However, in the case of PCLS-R(0//0), with significant discrepancies in both the initial and migrated delamination extents, the two stages were not as obvious as the others. In fact, the delamination at the initial 0°//0° interface exhibited a delayed progression compared to the migrated delamination at the 0°//90° interface. At the slow growth stage, the stiffness of the specimen shows a rapid increase, accompanied by a minor extent of delamination area. Subsequently, the onset of fast delamination growth led to a diminishing rate of stiffness increment. This phenomenon contrasts with the observations presented in [35], where a sudden decrease in stiffness, marked by a rapid increase in compliance, occurred with the extension of the delamination area. The difference can be mainly attributed to a different boundary condition, specifically whether boundary slippage is permitted or not. The current experimental setup precludes any form of slipping at the clamping area, leading to a persistent rise in stiffness.

Furthermore, similar delamination pattern was also depicted in PCLO specimens subjected to either single step or multi-step loadings. As shown in Fig. 11, a gradual onset of delamination growth occurs at a lower displacement level, followed by an accelerated propagation phase that commences at a higher displacement level, closer to the maximum loading.

4.3. Cross-sectional observation

Focusing on the embedded delamination growth, the typical planar delamination pattern evolved from the PTFE insert is illustrated in Fig. 12. The embedded delamination growth followed the ply orientation above the mid interface, while the migrated delamination growth aligned with the upper ply. The smaller semicircle shapes of delamination distributed at the diagonals were actually a second delamination migration. In order to provide a clearer understanding of the damage mechanisms, cross-sectional observation was performed for all specimens subjected to single step loading. The central cross section was chosen to be parallel to the ply orientation along which the initial delamination propagated ($A - A'$) or migrated ($B - B'$).

As shown in Fig. 13, the initial delamination propagated aligning with the fibres of the layer above the mid interface, corresponding to the rectangular part depicted in TOF C-scan. For PCLS(0//90) without rubber, except for the embedded delamination, multiple matrix cracks and delaminations occurred at different interfaces in both the upper and lower sub-laminates. In contrast, much less matrix cracks and delaminations occurred in PCLS-R specimens due to the rubber protection. For PCLO specimens, both intra-laminar and inter-laminar damage occurred at the contact region in the upper sub-laminates. Multiple delaminations evolved at the interfaces above the embedded delamination.

Despite the embedded delamination growth, an elongated delamination was formed at the top 1/2 interface for all specimens, shadowing the delaminations underneath it. In TOF C-scan, the elongated delamination at the top interface was shown in navy blue. Such delamination was initiated from the matrix crack at a lower layer and propagated along the fibre direction of the top layer. According to the DIC analysis, the elongated delamination propagated together with the embedded delamination growth, which eventually induced the surface crack at the top interface, causing significant stiffness degradation.

As measured by both C-scan and DIC (Fig. 8), the size of the embedded delamination growth of PCLS specimens was smaller than that of PCLO specimens. This can primarily be ascribed to the distinct fracture modes governing delamination growth in the two specimen configurations. In contrast to PCLO specimens, PCLS specimens exhibited a more extensive and densely distributed shear-induced micro-crack region (Fig. 14). In the case of PCLS specimens, the observed mode II delamination growth was a result of micro-crack coalescence near the crack front due to shearing [11,44]. A smaller region of shearing effect was presented in the PCLO specimen, indicating a shorter coalescence process. Furthermore, the interface also had influence on the formation of shear cracks. For PCLO(0//0), shearing-induced cracks remained undetected. The boundary between the two adjacent 0° layers exhibited

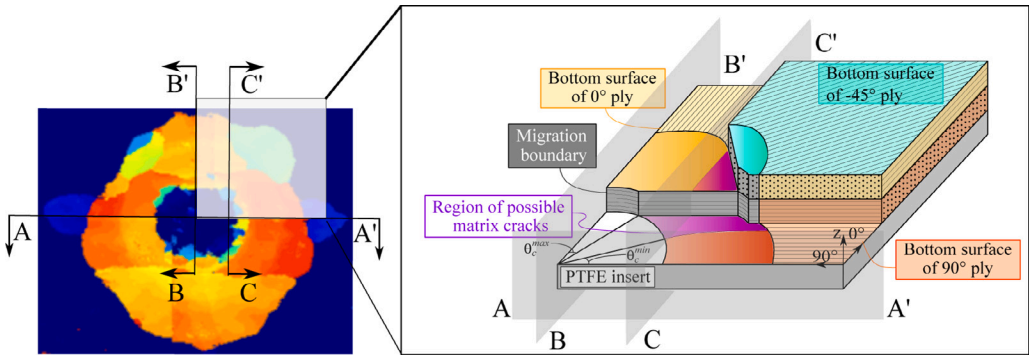

Fig. 12. Schematic of the typical planar delamination pattern.

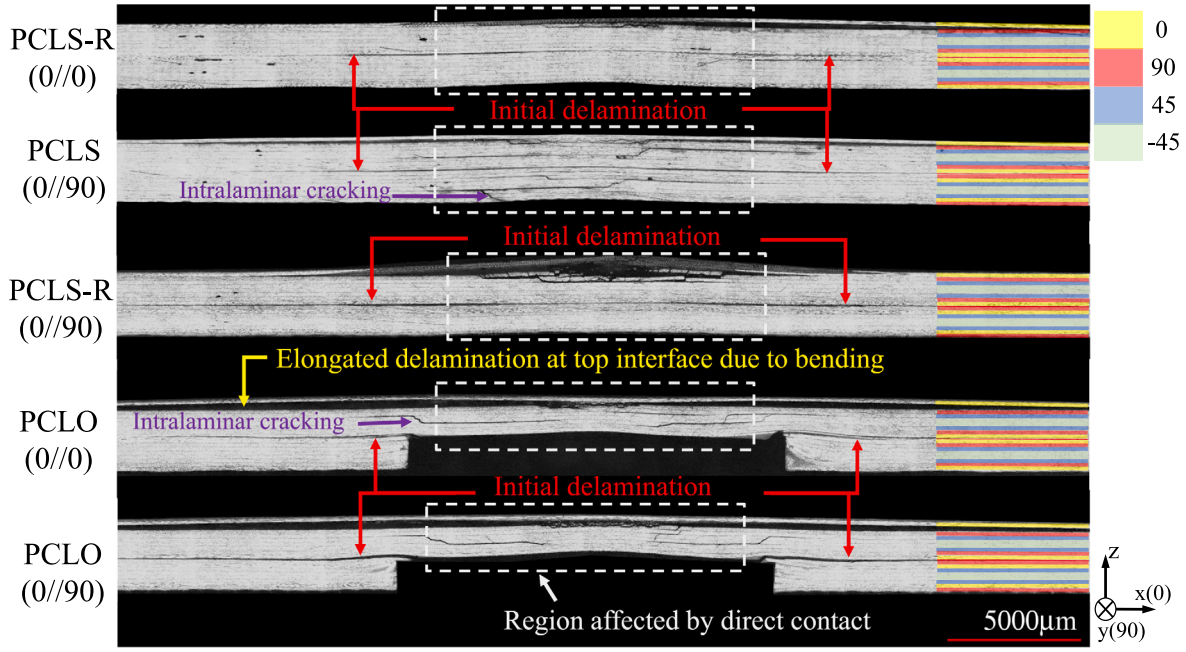

Fig. 13. Cross-sectional observation of delamination propagation in $A - A'$ cutting plane. The red arrows point at the tip of the embedded delamination.

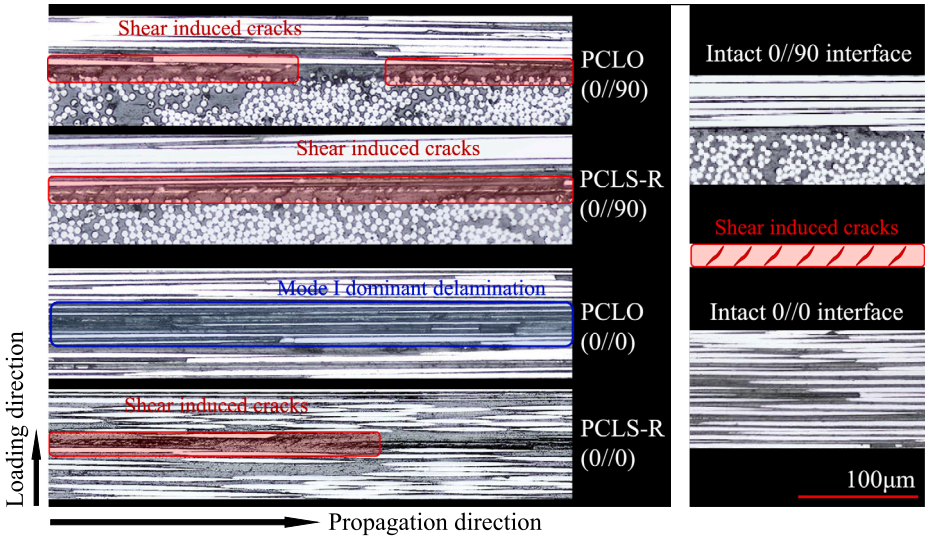

Fig. 14. Microscopic observation at the vicinity of the delamination front for all specimens.

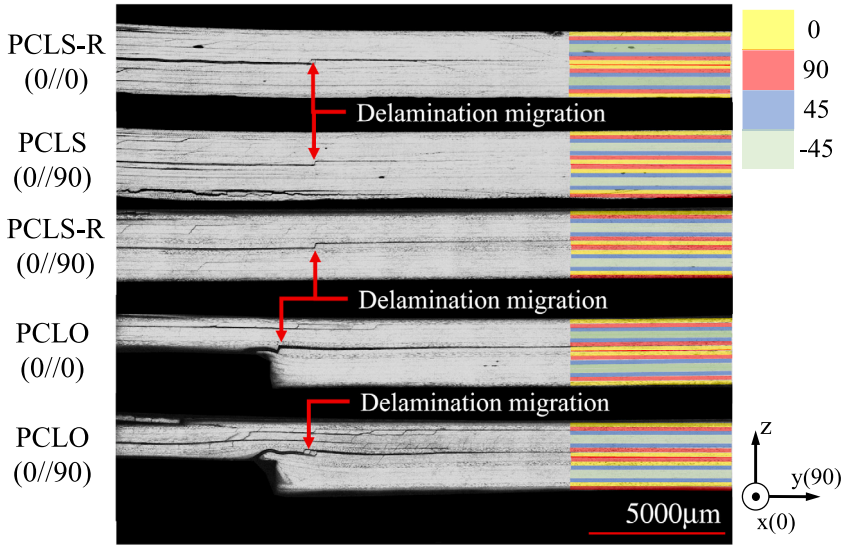

Fig. 15. Cross-sectional observation of delamination migration in $B - B'$ cutting plane. Note that the coordinate system indicating the actual fibre orientation is rotated by 90°, compared to A-A' cutting plane (Fig. 13).

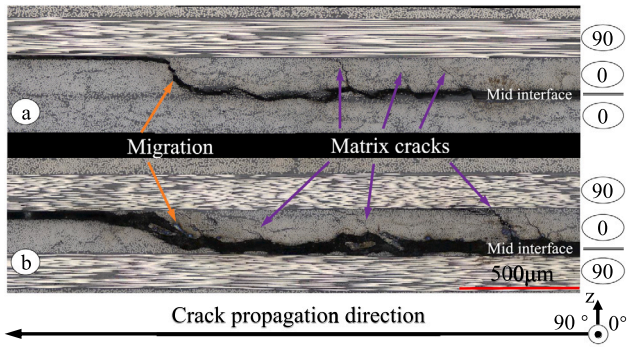

Fig. 16. Matrix cracks and delamination migration behaviours of (a) PCLS(0//0), (b) PCLO(0//90) specimens at C–C' cutting plane.

ambiguity. As depicted in Fig. 14, the intact 0° interface revealed a higher incidence of fibre nesting and a diminished presence of resin-rich regions where the shear cracks typically form. In contrast, at the 0°//90° interface, shear-induced matrix cracks were more prone to initiate and propagate within the resin-rich region, signifying a higher likelihood of micro-crack coalescence, which subsequently culminates in the formation of delamination.

The cutting plane $B - B'$ (Fig. 15) provides the observation of delamination migration at the embedded delamination front. For all specimens, migration initiated at the tip of the PTFE insert and then terminated at an upper interface where the directing crack plane was not parallel to the fibre direction. The observation verified that the two delamination regions observed from TOF C-scan corresponded to delamination growth at two adjacent interfaces. The initial delamination would propagate at the region where the fibre direction of the upper layer was parallel to the normal direction of the delamination boundary, but would migrate at the place where the fibre direction of the upper layer was perpendicular to the normal direction of the delamination boundary. As delamination propagated, the migrated delamination could again jump to an upper interface.

However, it was unclear, how the initial delamination propagated at the location where the fibre direction had a certain angle with the normal direction of the boundary. Therefore, the cutting plane $C - C'$ was used to explore the migration behaviour of a shifted cross section. As shown in Fig. 16, the initial delamination would propagate at the mid interface first. When the delamination joined with the major matrix crack, it would jump and then propagate at an upper interface. Although multiple matrix cracks were formed along the delamination path, migration was not induced immediately. According to Canturri [45], analysis of the local fracture mode provided more insights into the mechanisms of migration and delamination growth. Therefore, in this study, analysis of the local SERRs was also performed to present further interpretation for the observed planar delamination behaviour.

4.4. Determination of planar delamination initiation using AE

AE was used to provide a referable critical loading level for numerical investigation of planar delamination initiation. Multiple indicators can be utilized to detect damage commencement, for example the first high energy or high counts, the first increase in the gradient of accumulative energy or counts, or the first significant drop of the sentry function curve. However, which of those indicators provides the most accurate results is determined by the users' prior experience [46]. Since it was not the objective of this study to give a comprehensive understanding of the AE features and indicators, cumulative counts and cumulative energy were selected as they were sufficient for estimating the initiation of planar delamination.

As shown in Fig. 17, the accumulative AE counts and energy were plotted against the displacement recorded by the MTS machine, together with the applied force. In this particular analysis, the displacement is employed for all specimens since it provides an estimation of the applied critical displacement for numerical analysis. In the case of PCLS-R specimens, a notably reduced number of AE hits were recorded, indicating diminished damage attributed to the rubber protection. The corresponding displacement of the first substantial increase in the gradient of accumulative AE counts and energy was identified as the critical displacement for the numerical analysis. The determined critical displacements were summarized in Table 3. The first significant increase in the cumulative counts did not align with the pattern observed in cumulative energy for PCLS specimens. In fact, it was difficult to determine a distinct elevation in the cumulative counts, even when the curves were magnified for closer examination. This suggests that the cumulative counts curve displays lower sensitivity towards the initiation of delamination growth, specifically the formation of micro-cracks, yet exhibits a heightened sensitivity towards the rapid progression of delamination.

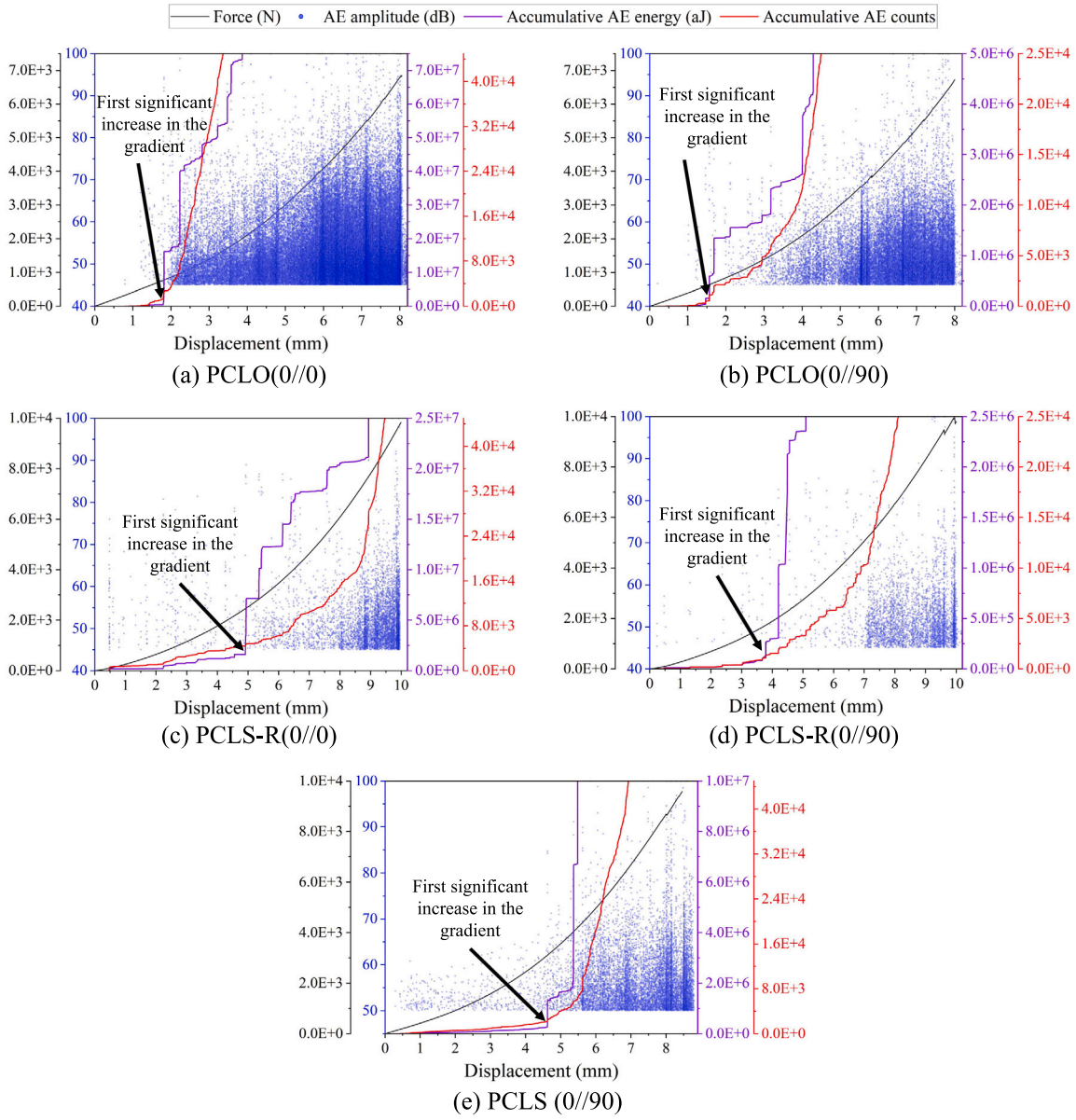

Fig. 17. Determination of the initiation of planar delamination in specimens with single-step loading: (a) PCLO(0//0), (b) PCLO(0//90), (c) PCLS-R(0//0), (d) PCLS-R(0//90), (e) PCLS(0//90). The curves of cumulative AE energy and counts are in magnified scale in order to determine the first significant increase in the gradient.

4.5. Numerical investigation

In order to investigate the mechanisms of the initiation of delamination and migration, analysis of the local SERR and stress state at the delamination front was conducted through finite element (FE) modelling using Abaqus/Standard. All the numerical results were extracted at the respective critical displacement level for the configuration being modelled, as given in Table 3.

As shown in Fig. 18, the predicted damage patterns, as visualized through cross-sectional views of the numerical models, exhibited similarity to the damage patterns observed in Fig. 13. The observed damage patterns can be considered as a consequence of progressions of the predicted damage modes. For PCLO specimens, different types of failure only occurred at the upper sub-laminates prior to delamination propagation. For PCLS(0//90) specimen lacking rubber protection, the occurrence of intra-laminar damage was apparent, particularly concentrated in the central region. Conversely, PCLS-R(0//0) specimen displayed significantly diminished predicted damage due to the rubber, which facilitated broader contact and, subsequently, a more uniform distribution of stress. For all specimens, matrix failure in the mid-upper ply predominantly occurred perpendicular to the upper ply orientation, serving as a primary factor contributing to the observed migration phenomenon.

The distribution of the local SERRs along the embedded delamination front was then analysed, as shown in Fig. 19. The overall local fracture mode for PCLS specimens was mainly mixed mode II/III. The pure G_{ii}, distributed following the upper ply orientation, dictated delamination growth, while pure G_{iii} induced delamination migration in the direction transverse to the upper ply orientation. For PCLO specimens, a localized mixture of mode I, mode II, and mode III was evident. Along the direction of delamination growth parallel to the fibres, a prevailing presence of mixed mode I and mode II was observed. Local mixed mode I and mode III dictated migration in the direction transverse to the upper ply orientation. The distribution of G_i aligning with the directing ply highlighted an elevated influence of mode I on the onset of delamination growth.

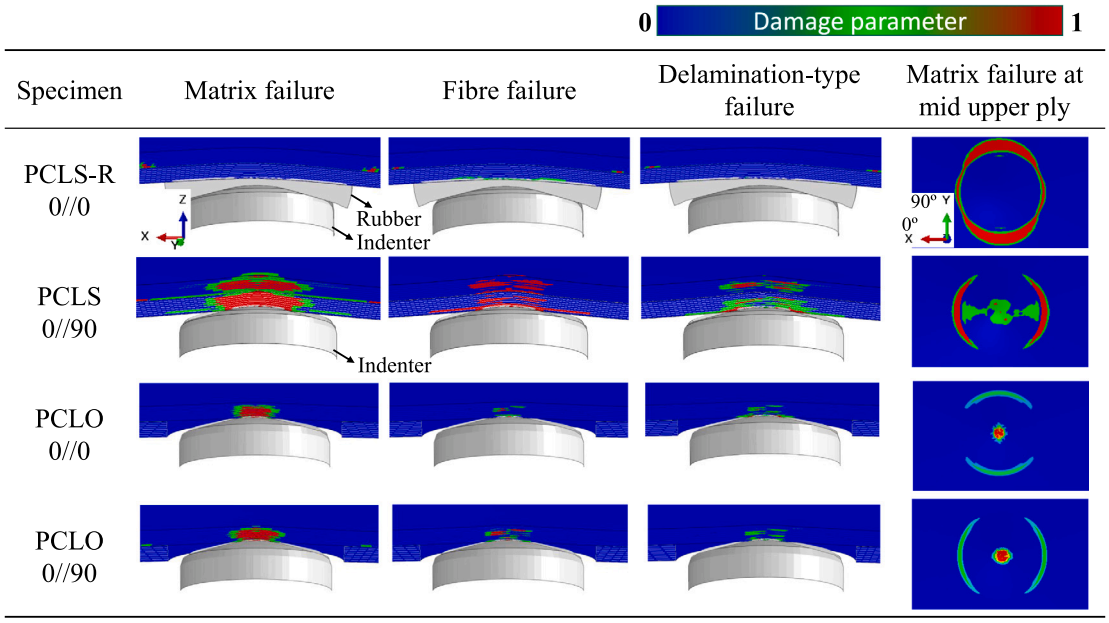

Fig. 18. Illustration of distinct damage patterns of different specimen configurations. The value of the damage variables corresponded to the severity of different failure modes. The predicted damage state corresponds to the critical displacement levels given in Table 3.

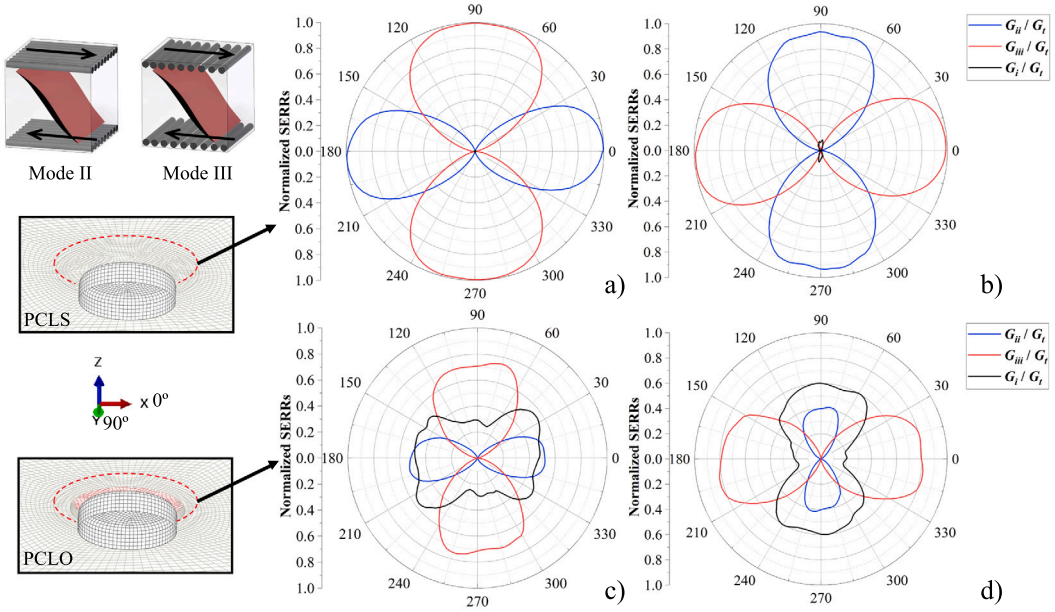

Fig. 19. Distributions of SERRs at the circular initial delamination front, overlayed on the ultrasonic scan results showing the delamination orientations: (a) PCLS-R(0//0), (b) PCLS(0//90), (c) PCLO(0//0), (d) PCLO(0//90). G_t indicates the total local SERR: $G_t = G_i + G_{ii} + G_{iii}$.

The stress tensors at the artificial delamination boundary were extracted, as shown in Fig. 20. Significant in-plane stretching (σ_{11}) was predicted in the direction of the fibre orientation. The maximum principal stress (MPS), overlapping with σ_{11}, is critical for delamination initiation. The shear induced micro cracks (Fig. 14) can be facilitated by a combination of σ_{13}, σ_{11} and σ_{33}. On the other hand, a combination of σ_{23}, σ_{22} and σ_{33} dictated delamination migration. The in-plane shear stress σ_{12} of a diagonal distribution could promote the inter-fibre matrix cracking along the fibre direction, thereby promoting the evolution of the migration boundary.

5. Discussion

5.1. Stiffening behaviour

According to the force–displacement behaviour and compliance analysis, a constant stiffening behaviour for all specimens subjected to single step loading was observed as shown in Figs. 3 and 4. The curves did not appear to be responding to the stiffness degradation due to delamination growth. One plausible explanation for this stiffening phenomenon can be attributed to the increasing external force required

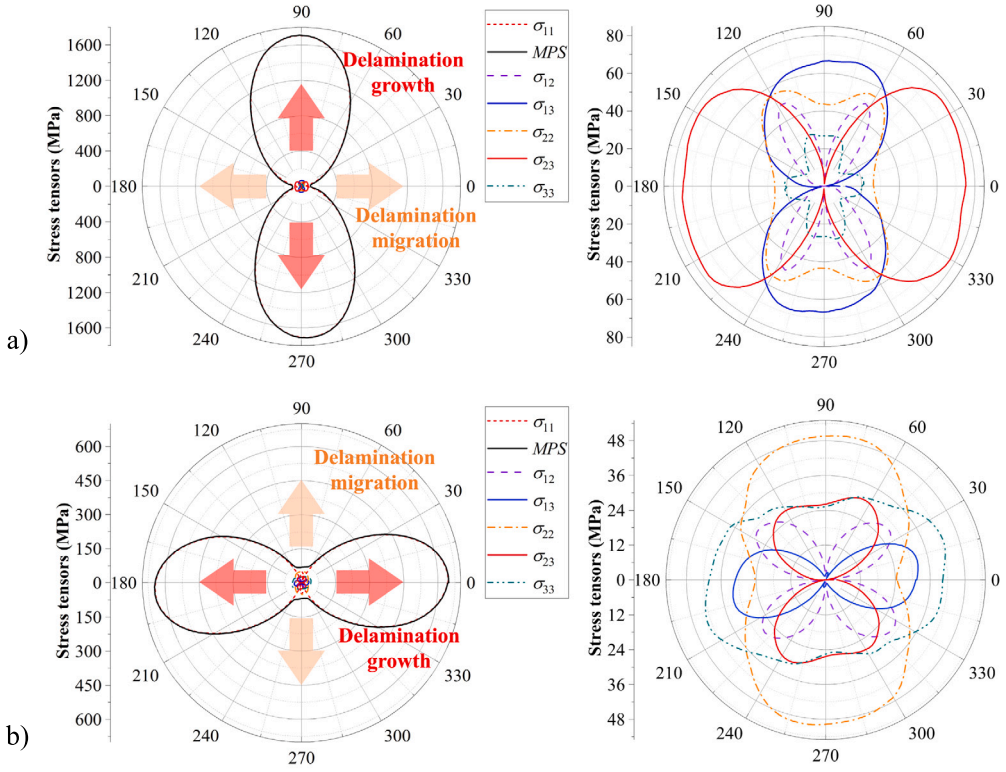

Fig. 20. Distributions of stress tensors at the circular initial delamination front: (a) PCLS(0//90), (b) PCLO(0//0).

Table 3
Critical displacement determination by AE. For PCLO(0//0), the lower prediction was adopted.

Specimen label	$\delta_{C,AE}$ (Accumulative energy)	$\delta_{C,AC}$ (Accumulative counts)
PCLO(0//0)	1.79 mm	1.77 mm
PCLO(0//90)	1.47 mm	1.47 mm
PCLS-R(0//0)	4.91 mm	–
PCLS-R(0//90)	3.79 mm	–
PCLS(0//90)	4.62 mm	–

to counterbalance caused by in-plane tension (or stretching) in the specimen. This would result in more elastic potential energy storage in the system. In contrast, only a relatively minor portion of energy dissipated, attributed to delamination growth and matrix cracking.

Moreover, 2-D delamination growth is multidirectional, signifying its advancement along contours. In contrast to the unidirectional delamination growth of beam-like specimens, such as double cantilever beam (DCB) or end notched flexure (ENF) configurations with uniform widths, the contour-wise delamination growth exhibits a nonlinear trend as the contour perimeter increases. By examining the energy dissipation on a per-unit-contour and per-unit-width basis, it becomes evident that the energy requisites for promoting unit contour-wise delamination growth are increasing, while the energy for unit width-wise delamination growth remain constant as the delamination propagates. Furthermore, the energy required for crack growth across distinct locations of the delamination contour exhibit variability, since the fracture energy is dependent on the mode mixity and interface angles, both of which exhibit variation along the contour. Consequently, the contour-wise delamination growth contributes to heightened fracture resistance. For instance, the last loading step of the multi-step tests has an enlarged "pre-crack" region due to the advancement of the initial delamination (Fig. 10). The expansion of a larger delamination area demands increased external force, thereby inducing augmented in-plane stretching that contributes to the observed stiffening behaviour (Figs. 5 and 6).

Additionally, fibre bridging, which could potentially occur at the delaminated interfaces, could also contribute to the stiffening mechanism [33,35]. However, no evidential bridging effects were demonstrated in the current experiment with CFRP composite laminates. A more insightful understanding of the bridging effect could potentially be achieved through fractographic examinations, which yield valuable insights into the crack surface characteristics.

5.2. Mechanisms of planar delamination propagation and migration

From the experimental observation, delamination growth seemed to be dependent on the interface properties such as the fibre orientations and the composition of the resin and fibres along the delamination front. Despite those, the overall delamination patterns of different specimen configurations were rather similar.

As illustrated in Fig. 12, delamination growth in the middle or migrated interface was directed by the fibre orientation of the upper ply. The major matrix crack, initiated at the boundary of the PTFE insert, would propagate in the directing ply, causing a migration boundary. The migrated delamination could again jump to an upper interface as external loading increased. Hypothetically, an upper limit θ_{max} for the occurrence of migration and a lower limit θ_{min} for delamination growth can be characterized. Matrix cracks may occur in the range between θ_{max} and θ_{min}, but no migration would be triggered. The embedded delamination would traverse the intra-laminar matrix cracks, creating a more critical crack front and thus preventing delamination migration. Similar findings were also presented in Canturri's study of buckle-driven delamination [25].

The calculated local SERRs and stress tensors may offer a solely qualitative analysis of the driving force governing the initiation of progression and migration of planar delamination, rather than being

sufficient to quantitatively characterize the actual fracture energy and to determine the driving force for planar delamination growth. A reliable numerical or analytical method is indispensable for acquiring an intrinsic comprehension of the delamination behaviour. Since the present study did not encompass the comprehensive modelling of the progressive damage evolution, a prospective avenue for future research involves the development of an approach adept at capturing both matrix and delamination expansions. This could be achieved by incorporating CZM to simulate interlaminar delamination and utilizing an energy method-based criterion to predict intralaminar damage evolution [47].

6. Conclusions

In this study, a novel experimental method was developed to investigate the planar delamination behaviour of CFRP composite laminates under quasi-static out-of-plane loading. The planar delamination pattern was captured using DIC analysis, C-scan and cross-sectional microscopy. Numerical investigation of the local SERR and stress distributions provided insights into the mechanisms of delamination growth and migration phenomena in the CFRP panel. The following aspects can be concluded based on the experimental and numerical investigation:

- Despite the progression of the artificially embedded delamination, a consistent trend of stiffening was observed due to in-plane stretching. Two discernible stages within the planar delamination behaviour are revealed: a slow growth stage marked by a rapid increase in stiffness, followed by a subsequent stage of accelerated delamination growth with a comparatively more gradual increase in stiffness. Consequently, the force–displacement behaviour proved inadequate for detecting and characterizing delamination growth.
- The fibre orientation and composition of the fibres and matrix at the delamination front possess significant influence on the development of shear-induced microcracks, thus affecting the delamination pattern. The artificially embedded delamination propagated in the direction where the fibre orientation of the layer above the crack interface was parallel, but initially migrated to an upper interface at the place where the fibre was perpendicular. Delamination migration would continue to extend parallel to the fibre direction within the directing ply, creating a migration boundary below which delamination migration is inhibited.
- For shear dominant delamination, local mode II was found to stimulate delamination growth aligning to the directing ply orientation, while delamination migration perpendicular to the ply orientation was induced by local mode III. In combined opening-shear mode, a more pronounced influence of mode I on delamination growth was evident.

Further investigation on the tomography of the delamination surface holds the potential to yield a comprehensive understanding of the planar delamination mechanisms. This investigation is slated for subsequent studies. Moreover, a numerical model capable of quantitatively characterizing planar delamination growth and migration will also be developed, which may aid in the evaluation of fracture tolerance and design of composite structures.

CRediT authorship contribution statement

Wenjie Tu: Writing – review & editing, Writing – original draft, Methodology, Investigation, Formal analysis, Data curation, Conceptualization. **John-Alan Pascoe:** Writing – review & editing, Supervision, Methodology, Conceptualization. **René Alderliesten:** Writing – review & editing, Supervision, Resources, Methodology, Conceptualization.

Declaration of competing interest

The authors declare that they have no known competing financial interests or personal relationships that could have appeared to influence the work reported in this paper.

Data availability

Research data is available at 4TU.ResearchData: https://doi.org/10.4121/8ca918e1-4423-499e-be19-174562fa6973.

Acknowledgements

The authors gratefully acknowledge the financial support from the China Scholarship Council, China (No. CSC202006950073).

References

[1] O'Brien TK. Mixed-mode strain-energy-release rate effects on edge delamination of composites. ASTM Special Technical Publication; 1984, p. 125–42. http://dx.doi.org/10.1520/stp30201s.
[2] Reddy J. Mechanics of laminated composite plates and shells: Theory and analysis. CRC Press; 2003, http://dx.doi.org/10.1201/b12409.
[3] ASTM D5528-01. Standard test method for mode I interlaminar fracture toughness of unidirectional fiber-reinforced polymer matrix composites. Am Stand Test Methods 2014;03(Reapproved 2007):1–12. http://dx.doi.org/10.1520/D5528-13.2.
[4] ASTM D7905. Standard test method for determination of the mode II interlaminar fracture toughness of unidirectional fiber-reinforced polymer matrix composites. ASTM; 2014, p. 1–18. http://dx.doi.org/10.1520/D7905.
[5] ASTM D6671M. Standard test method for mixed mode I-Mode II interlaminar fracture toughness of unidirectional fiber reinforced polymer matrix composites. ASTM; 2006, p. 15.
[6] Greenhalgh ES, Rogers C, Robinson P. Fractographic observations on delamination growth and the subsequent migration through the laminate. Compos Sci Technol 2009;69(14):2345–51. http://dx.doi.org/10.1016/j.compscitech.2009.01.034.
[7] Gong Y, Zhang B, Hallett SR. Delamination migration in multidirectional composite laminates under mode I quasi-static and fatigue loading. Compos Struct 2018;189:160–76. http://dx.doi.org/10.1016/j.compstruct.2018.01.074.
[8] Pichler N, Herráez M, Botsis J. Mixed-mode fracture response of anti-symmetric laminates: Experiments and modelling. Composites B 2020;197:108089. http://dx.doi.org/10.1016/j.compositesb.2020.108089.
[9] Hu P, Tao R, Li X, Lubineau G. Decomposing the coupling damage in mode I multidirectional delamination. Compos Sci Technol 2022;229:109684. http://dx.doi.org/10.1016/j.compscitech.2022.109684.
[10] Gong Y, Zhang B, Mukhopadhyay S, Hallett SR. Experimental study on delamination migration in multidirectional laminates under mode II static and fatigue loading, with comparison to mode i. Compos Struct 2018;201:683–98. http://dx.doi.org/10.1016/j.compstruct.2018.06.081.
[11] Amaral L, Alderliesten R, Benedictus R. Towards a physics-based relationship for crack growth under different loading modes. Eng Fract Mech 2018;195:222–41. http://dx.doi.org/10.1016/j.engfracmech.2018.04.017.
[12] Laksimi A, Ahmed Benyahia A, Benzeggagh M, Gong X. Initiation and bifurcation mechanisms of cracks in multi-directional laminates. Compos Sci Technol 2000;60(4):597–604. http://dx.doi.org/10.1016/S0266-3538(99)00179-7.
[13] Hu X, Chen B, Tirvaudey M, Tan V, Tay T. Integrated XFEM-CE analysis of delamination migration in multi-directional composite laminates. Composites A 2016;90:161–73. http://dx.doi.org/10.1016/j.compositesa.2016.07.007.
[14] Chen B, Tay T, Pinho S, Tan V. Modelling delamination migration in angle-ply laminates. Compos Sci Technol 2017;142:145–55. http://dx.doi.org/10.1016/j.compscitech.2017.02.010.
[15] van der Panne M. Effect of different fibre orienta- tions at the interface on fatigue delamination growth [Ph.D. thesis], Delft University of Technology; 2022, p. 73.
[16] Hu P, Pulungan D, Tao R, Lubineau G. An experimental study on the influence of intralaminar damage on interlaminar delamination properties of laminated composites. Composites A 2020;131:105783. http://dx.doi.org/10.1016/j.compositesa.2020.105783.
[17] Shi Y, Hull D, Price J. Mode II fracture of $+\theta/-\theta$ angled laminate interfaces. Compos Sci Technol 1993;47(2):173–84. http://dx.doi.org/10.1016/0266-3538(93)90045-I.
[18] Herráez M, Pichler N, Pappas G, Blondeau C, Botsis J. Experiments and numerical modelling on angle-ply laminates under remote mode II loading. Composites A 2020;134:105886. http://dx.doi.org/10.1016/j.compositesa.2020.105886.
[19] Ratcliffe JG, Czabaj MW, O'brien TK. A test for characterizing delamination migration in carbon/epoxy tape laminates. In: NASA technical reports. 2012, p. 19.

[20] Mollenhauer D, Zhou E, Hoos K, Iarve E, Braginsky M, Breitzman T, Rapking D. Multi-scale simulation of delamination migration. In: Proceedings of the American society for composites - 31st technical conference. 2016, p. 10.
[21] Ramji A, Xu Y, Yasaee M, Grasso M, Webb P. Delamination migration in CFRP laminates under mode I loading. Compos Sci Technol 2020;190:108067. http://dx.doi.org/10.1016/j.compscitech.2020.108067.
[22] Quan D, Liu J, Yao L, Dransfeld C, Alderliesten R, Zhao G. Interlaminar and intralaminar fracture resistance of recycled carbon fibre/PPS composites with tailored fibre/matrix adhesion. Compos Sci Technol 2023;239:110051. http://dx.doi.org/10.1016/j.compscitech.2023.110051.
[23] Yao L, Liu J, Lyu Z, Alderliesten R, Hao C, Ren C, et al. In-situ damage mechanism investigation and a prediction model for delamination with fibre bridging in composites. Eng Fract Mech 2023;281:109079. http://dx.doi.org/10.1016/j.engfracmech.2023.109079.
[24] Canturri C, Greenhalgh ES, Pinho ST, Ankersen J. Delamination growth directionality and the subsequent migration processes – The key to damage tolerant design. Composites A 2013;54:79–87. http://dx.doi.org/10.1016/j.compositesa.2013.07.004.
[25] Canturri C, Greenhalgh ES, Asp LE, Pinho ST. Fractographic study to characterise the interaction between intralaminar and interlaminar fracture from embedded defects under compression loading. Composites A 2019;125:105557. http://dx.doi.org/10.1016/j.compositesa.2019.105557.
[26] Whitcomb JD. Parametric analytical study of instability-related delamination growth. Compos Sci Technol 1986;25(1):19–48. http://dx.doi.org/10.1016/0266-3538(86)90019-9.
[27] Nilsson K-F, Thesken J, Sindelar P, Giannakopoulos A, Stoåkers B. A theoretical and experimental investigation of buckling induced delamination growth. J Mech Phys Solids 1993;41(4):749–82. http://dx.doi.org/10.1016/0022-5096(93)90025-B.
[28] Bolotin VV. Delaminations in composite structures: Its origin, buckling, growth and stability. Composites B 1996;27(2):129–45. http://dx.doi.org/10.1016/1359-8368(95)00035-6.
[29] Nilsson K-F, Asp L, Alpman J, Nystedt L. Delamination buckling and growth for delaminations at different depths in a slender composite panel. Int J Solids Struct 2001;38(17):3039–71. http://dx.doi.org/10.1016/S0020-7683(00)00189-X.
[30] Köllner A, Völlmecke C. An analytical framework to extend the general structural stability analysis by considering certain inelastic effects—theory and application to delaminated composites. Compos Struct 2017;170:261–70. http://dx.doi.org/10.1016/j.compstruct.2017.01.088.
[31] Köllner A. Predicting buckling-driven delamination propagation in composite laminates: An analytical modelling approach. Compos Struct 2021;266:113776. http://dx.doi.org/10.1016/j.compstruct.2021.113776.
[32] Köllner A, Nielsen MW, Srisuriyachot J, Rhead AT, Butler R. Buckle-driven delamination models for laminate strength prediction and damage tolerant design. Thin-Walled Struct 2021;161:107468. http://dx.doi.org/10.1016/j.tws.2021.107468.
[33] Cameselle-Molares A, Vassilopoulos AP, Renart J, Turon A, Keller T. Numerical simulation of two-dimensional in-plane crack propagation in FRP laminates. Compos Struct 2018;200:396–407. http://dx.doi.org/10.1016/j.compstruct.2018.05.136.
[34] Cameselle-Molares A, Vassilopoulos AP, Keller T. Experimental investigation of two-dimensional delamination in GFRP laminates. Eng Fract Mech 2018;203:152–71. http://dx.doi.org/10.1016/j.engfracmech.2018.05.015.
[35] Wang C, Vassilopoulos AP, Keller T. Experimental investigation of two-dimensional Mode-II delamination in composite laminates. Composites A 2023;173:107666. http://dx.doi.org/10.1016/j.compositesa.2023.107666.
[36] Chatterjee SN, Dick WA, Byron Pipes R. Mixed-mode delamination fracture in laminated composites. Compos Sci Technol 1986;25(1):49–67. http://dx.doi.org/10.1016/0266-3538(86)90020-5.
[37] Den Ouden HJ. Investigating planar delamination behavior in carbon fiber reinforced polymer panels an evaluation of delamination criteria [Ph.D. thesis], Delft University of Technology; 2020.
[38] Delta-tech. Matrix technical data sheet - DT120 versatile high toughness epoxy matrix. Tech. rep, Delta-tech; 2015.
[39] Lord S, Greenhalgh E. Modelling of delamination and debonding in laminated composites using a moving mesh approach. In: 11th European conference on composite materials. 2004, p. 10.
[40] Tserpes KI, Papanikos P, Kermanidis T. A three-dimensional progressive damage model for bolted joints in composite laminates subjected to tensile loading. Fatigue Fract Eng Mater Struct 2001;24(10):663–75. http://dx.doi.org/10.1046/j.1460-2695.2001.00424.x.
[41] Abaqus inc. SIMULIA user assistance 2021, Abaqus user subroutines guide. 2021.
[42] Huo L, Kassapoglou C, Alderliesten R. A criterion for predicting delamination growth in composite laminates. Mater Des 2022;223:111160. http://dx.doi.org/10.1016/j.matdes.2022.111160.
[43] Li X, Liang B, Liu P, Cheng H, Cao S, Zhang K. Experimental and numerical analysis of low-velocity impact damage of CFRP laminates with rubber protective layer. Compos Struct 2022;300:116152. http://dx.doi.org/10.1016/j.compstruct.2022.116152.
[44] Quan D, Urdániz JL, Ivanković A. Enhancing mode-I and mode-II fracture toughness of epoxy and carbon fibre reinforced epoxy composites using multi-walled carbon nanotubes. Mater Des 2018;143:81–92. http://dx.doi.org/10.1016/j.matdes.2018.01.051.
[45] Canturri C, Greenhalgh ES, Pinho ST. The relationship between mixed-mode II/III delamination and delamination migration in composite laminates. Compos Sci Technol 2014;105:102–9. http://dx.doi.org/10.1016/j.compscitech.2014.10.001.
[46] Saeedifar M, Zarouchas D. Damage characterization of laminated composites using acoustic emission: A review. Composites B 2020;195:108039. http://dx.doi.org/10.1016/j.compositesb.2020.108039.
[47] Socci CA, Kassapoglou C. Prediction of matrix crack initiation and evolution and their effect on the stiffness of laminates with off-axis plies under in-plane loading. Compos Sci Technol 2020;200:108427. http://dx.doi.org/10.1016/j.compscitech.2020.108427.